

Fig. 2. (a) Cumulative computation energy up to each layer of AlexNet. (b) Number of bits of compressed output data at each layer to be transmitted to the cloud.

involves no communication but drains its battery during the energy-intensive computation.

Computation partitioning between the client and the cloud represents a middle ground: the computation is partially processed *in situ*, up to a specific CNN layer, on the client. The data are then transferred to the cloud to complete the computation, after which the inference results are sent back to the client, as necessary. We propose NeuPart, a partitioner for DL tasks that minimizes client energy. NeuPart is based on an analytical modeling framework, and analytically identifies, *at runtime*, the energy-optimal partition point at which the partial computation on the client is sent to the cloud.

Fig. 2 concretely illustrates the tradeoff between communication and computation for AlexNet. In (a), we show the cumulative computation energy (obtained from our analytical CNN energy model presented in Section IV) from the input to a specific layer of the network. In (b), we show the volume of compressed data that must be transmitted when the partial *in situ* computation is transmitted to the cloud. The data computed in internal layers of the CNN tend to have significant sparsity (over 80%, as documented later in Fig. 10): NeuPart leverages this sparsity to transmit only nonzero data at the point of partition, thus limiting the communication cost.

The net energy cost for the client for a partition at the L^{th} layer can be computed as follows:

$$E_{\text{Cost}} = E_L + E_{\text{Trans}} \quad (1)$$

where E_L is the processing energy on the client, up to the L^{th} CNN layer, and E_{Trans} is the energy required to transmit this partially computed data from the client to the cloud. The inference result corresponds to a trivial amount of data to return the identified class and involves negligible energy.

NeuPart focuses on minimizing E_{Cost} for the energy-constrained client. For the data in Fig. 2, E_L increases monotonically as we move deeper into the network, but E_{Trans} can reduce greatly. Thus, the optimal partitioning point for E_{Cost} here lies at an intermediate layer L .

B. Contributions of NeuPart

The specific contributions of NeuPart are twofold.

- 1) We develop a new analytical energy model (we name our model “CNNergy,” which is the core of NeuPart) to estimate the energy of executing CNN workload (i.e., E_L) on an ASIC-based DL accelerator.

- 2) Unlike prior computation partitioning works [7]–[12], NeuPart addresses the client/cloud partitioning problem for specialized DL accelerators that are more energy-efficient than CPU/GPU/FPGA-based platforms. Today, neural networks are driving research in many fields, and customized neural hardware is possibly the most active area in IC design research. While there exist many simulation platforms for performance analysis for general-purpose processors [13], memory systems [14], and NoCs [15], there is no comparable performance simulator for ASIC implementations of CNNs. Our model, CNNergy, is an attempt to fill that gap. CNNergy accounts for the complexities of scheduling computations over multidimensional data. It captures key parameters of the hardware and maps the hardware to perform computation on various CNN topologies. CNNergy is benchmarked on several CNNs: AlexNet, SqueezeNet-v1.1 [16], VGG-16 [17], and GoogleNet-v1 [18]. CNNergy is far more detailed than prior energy models [19] and incorporates implementation-specific details of a DL accelerator, capturing all major components of the *in situ* computation, including the cost of arithmetic computations, memory and register access, control, and clocking. It is important to note that for an ASIC-based neural accelerator platform, unlike a general-purpose processor, the computations are highly structured and the memory fetches are very predictable. Unlike CPUs, there are no conditionals or speculative fetches that can alter program flow significantly. Therefore, an analytical modeling framework (as validated in Section V) is able to predict the CNN energy consumption closely for the custom ASIC platform.

CNNergy may potentially have utility beyond this article and has been open-sourced at <https://github.com/manasiumn37/CNNergy>. For example, it provides a breakdown of the total energy into specific components, such as data access energy from different memory levels of a DL accelerator, data access energy associated with each CNN data type from each level of memory, and multiply-accumulate (MAC) computation energy. CNNergy can also be used to explore design phase tradeoffs such as analyzing the impact of changing on-chip memory size on the total execution energy of a CNN. We believe that our developed simulator (CNNergy) will be useful to the practitioners who need an energy model for CNNs to evaluate various design choices. The application of data partitioning between client and cloud shows a way to apply our energy model to a practical scenario.

This article is organized as follows. Section II discusses prior approaches to computational partitioning and highlights the differences of NeuPart as compared to the prior works. In Section III, fundamental background on CNN computation is provided, and the general framework of CNNergy for CNN energy estimation on custom ASIC-based DL accelerators is outlined. Next, Section IV presents the detailed modeling of CNNergy and is followed by Section V, which validates the model in several ways, including against silicon data. Section VI presents the models for the estimation of transmission energy as well as inference delay. A method for performing the NeuPart client/cloud partitioning at runtime is discussed in Section VII. Finally, in Section VIII,

the evaluations of the client/cloud partitioning using NeuPart are presented under various communication environments for widely used CNN topologies. This article concludes in Section IX.

II. RELATED WORK

Computational partitioning has previously been used in the general context of distributed processing [20]. A few prior works [7]–[12] have utilized computation partitioning in the context of mobile DL. In [7], tasks are offloaded to a server from nearby Internet of things (IoT) devices for best server utilization, but no attempt is made to minimize edge device energy. In [8] and [9], partitioning is used to optimize overall delay or throughput for delay critical applications of deep neural network (DNN) (e.g., self-driving cars [8]). Another work [10] uses partitioning between the client and the local server (in contrast to the centralized cloud), where, along with the inference data, the client also needs to upload the partial DNN model (i.e., DNN weights) to the local server every time it makes an inference request. Therefore, the optimization goals and the target platforms of these works are very different from NeuPart.

The work in [11] uses limited application-specific profiling data to schedule computation partitioning. Another profiling-based scheme [12] uses client-specific profiling data to form a regression-based computation partitioning model for each device. A limitation of profiling-based approaches is that they require profiling data for each mobile device or each DL application, which implies that a large number of profiling measurements are required for real-life deployment. Moreover, profiling-based methods require the hardware to already be deployed and cannot support design-phase optimizations. Furthermore, all these prior approaches use a CPU/GPU-based platform for the execution of DL workloads.

In contrast with prior methods, NeuPart works with specialized DL accelerators, which are orders of magnitude more energy-efficient as compared to the general-purpose machines [1], [21], [22], for client/cloud partitioning. NeuPart specifically leverages the highly structured nature of computations on CNN accelerators and shows that an analytical model predicts the client energy accurately (as demonstrated in Section V). The analytical framework used in the NeuPart CNNErgy incorporates implementation-specific details that are not modeled in prior works. For example, the work in Neurosurgeon [12] uses 1) uncompressed raw image to transmit at the input, which is not typical: in a real system, images are compressed before transmission to reduce the communication overhead; 2) unequal bit width (i.e., 32-bit data for the intermediate layers while 8-bit data for the input layer); and 3) ignores any data sparsity at the intermediate CNN layers. Consequently, these cause the partitioning decision by Neurosurgeon to be either client-only or cloud-only in most cases. In contrast, in addition to using a specialized DL accelerator, NeuPart fully leverages the inherent computation–communication tradeoff of CNNs by exploiting their key properties and shows that (Fig. 13) there is a wide space where an intermediate partitioning point can offer significant energy savings as compared to the client-only or cloud-only approaches.

TABLE I
PARAMETERS FOR A CNN LAYER SHAPE

Parameters	Description
R/S	Height/width of a filter
H/W	Padded height/width of an ifmap
E/G	Height/width of an ofmap
C	#of channels in an ifmap and filter
F	#of 3D filters in a layer #of channels in an ofmap
U	Convolution stride

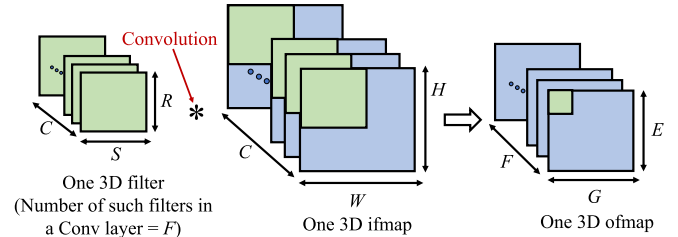


Fig. 3. Illustration of ifmap, filter, and ofmap in a Conv layer.

III. COMPUTATIONS ON CNN HARDWARE

A. Fundamentals of CNNs

The computational layers in CNNs can be categorized into three types: convolution (Conv), fully connected (FC), and pooling (Pool). The computation in a CNN is typically dominated by the Conv layers. In each layer, the computation involves three types of data:

- 1) ifmap: the input feature map;
- 2) filter: the filter weights;
- 3) psum: the intermediate partial sums.

Table I summarizes the parameters associated with a Conv layer. As shown in Fig. 3, for a **Conv layer**, filter and ifmap are both 3-D data types consisting of multiple 2-D planes (channels). Both the ifmap and filter have the same number of channels, C , while $H \gg R$ and $W \gg S$.

During the convolution, an elementwise multiplication between the filter and the green 3-D region of the ifmap in Fig. 3 is followed by the accumulation of all products (i.e., psums) and results in one element shown by the green box in the output feature map (ofmap). Each channel ($R \times S \times 1$) of the filter slides through its corresponding channel ($W \times H \times 1$) of the ifmap with a stride (U), repeating similar MAC operations to produce a full 2-D plane ($E \times G \times 1$) of the ofmap. A nonlinear activation function (e.g., a rectified linear unit, ReLU) is applied after each layer, introducing sparsity (i.e., zeros) at the intermediate layers, which can be leveraged to reduce computation.

The abovementioned operation is repeated for all F filters to produce F 2-D planes for the ofmap, i.e., the number of channels in the ofmap equals the number of 3-D filters in that layer. Due to the nature of the convolution operation, there is ample opportunity for data reuse in a Conv layer. **FC layers** are similar to Conv layers but are smaller in size and produce a 1-D ofmap. Computations in the **Pool layers** serve to reduce the dimensionality of the ofmaps produced from the Conv layers by storing the maximum/average value over a window of the ofmap.

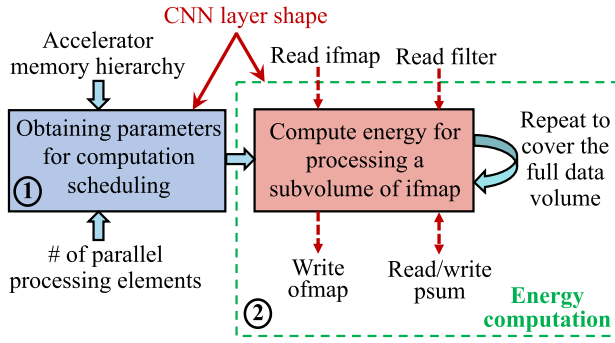


Fig. 4. General framework of the analytical CNN energy model (CNNergy).

B. Executing CNN Computations on a Custom ASIC

1) Architectural Features of CNN Hardware Accelerators:

Since the inference task of a CNN comprises a very structured and fixed set of computations (i.e., MAC, nonlinear activation, pooling, and data access for the MAC operands), specialized hardware accelerators are very suitable for their execution. Various dedicated accelerators have been proposed in the literature for the efficient processing of CNNs [1], [22]–[26]. The architecture in Google tensor processing unit (TPU) [1] consists of a 2-D array of parallel MAC computation units, a large on-chip buffer for the storage of ifmap and psum data, additional local storage inside the MAC computation core for the filter data, and finally, off-chip memory to store all the feature maps and filters together. Similarly, along with an array of parallel processing elements (PEs), the architectures in [22], [24], [25], and [26] use a separate on-chip SRAM to store a chunk of filter, ifmap, and psum data, and an external DRAM to completely store all the ifmap/ofmap and filter data. In [22] and [23], local storage is used inside each PE while allowing data communication between PEs to facilitate better reuse of data. In addition, Chen *et al.* [23], Aimar *et al.* [25], and Sim *et al.* [26] exploit the inherent data sparsity in the internal layers of CNN to save computation energy.

It is evident that the key architectural features of these accelerators are fundamentally similar: an array of PEs to perform neural computation in parallel, multiple levels of memory for fast data access, and greater data reuse. We utilize these key architectural features of ASIC hardware to develop the general framework of CNNergy.

2) *General Framework of CNNergy*: We develop CNNergy to estimate the energy dissipation in a CNN hardware accelerator. The general framework of CNNergy is illustrated in Fig. 4. We use CNNergy to determine the *in situ* computation energy [E_L in (1)], accounting for scheduling and computation overheads.

One of the largest contributors to energy is the cost of data access from memory. Thus, data reuse is critical for energy-efficient execution of CNN computations to reduce unnecessary high-energy memory accesses, particularly the ifmap and filter weights, and is used in [1], [22], [23], [25] and [26]. This may involve, for example, ifmap and filter weight reuse across convolution windows, ifmap reuse across filters, and reduction of psum terms across channels. Given the accelerator memory hierarchy, the number of parallel PEs,

and CNN layer shape, Block ① of Fig. 4 is an automated scheme for scheduling MAC computations while maximizing data reuse. The detailed methodology for obtaining these scheduling parameters is presented in Section IV-C.

Depending on the scheduling parameters, the subvolume of the ifmap to be processed at a time is determined. Then, Block ② computes the corresponding energy for the MAC operations and associated data accesses. The computation in Block ② is repeated to process the entire data volume in a layer, as detailed in Section IV-D.

The framework of CNNergy is general and its principles apply to a large class of CNN accelerators. However, to validate the framework, we demonstrate it on a specific platform, Eyeriss [23], for which ample performance data are available, including silicon measurements. Eyeriss has an array of $J \times K$ PEs, each with the following:

- 1) an MAC computation unit;
- 2) register files (RFs) for filter, ifmap, and psum data.

We define f_s , I_s , and P_s as the maximum number of b_w -bit filter, ifmap, and psum elements that can be stored in a PE.

The accelerator consists of four levels of memory: DRAM, global SRAM buffer (GLB), inter-PE RF access, and local RF within a PE. During the computations of a layer, filters are loaded from DRAM to RF. In the GLB, storage is allocated for psum and ifmap. After loading data from DRAM, ifmaps are stored into the GLB to be reused from the RF level. The irreducible psums navigate through GLB and RF as needed. After complete processing of a 3-D ifmap, the ofmaps are written back to DRAM.

IV. ANALYTICAL CNN ENERGY MODEL

We formulate an analytical model (CNNergy) for the CNN processing energy [used in (1)], E_L , up to the L^{th} layer, as

$$E_L = \sum_{i=1}^L E_{\text{Layer}}(i) \quad (2)$$

where $E_{\text{Layer}}(i)$ is the energy required to process layer i of the CNN. To keep the notation compact, we drop the index “(i)” in the remainder of this section. We can write E_{Layer} as

$$E_{\text{Layer}} = E_{\text{Comp}} + E_{\text{Ctrl}} + E_{\text{Data}} \quad (3)$$

where E_{Comp} is the energy to compute MAC operations associated with the i^{th} layer, E_{Ctrl} represents the energy associated with the control and clocking circuitry in the accelerator, and E_{Data} is the memory data access energy

$$E_{\text{Data}} = E_{\text{onChip-data}} + E_{\text{DRAM}} \quad (4)$$

i.e., the sum of data access energy from on-chip memory (from GLB, Inter-PE, and RF) and the off-chip DRAM.

The computation of these energy components, particularly the data access energy, is complicated by their dependence on the data reuse pattern in the CNN. In Sections IV-A–IV-D, we develop a heuristic for optimal data reuse and describe the methodology in our CNNergy for estimating these energy components.

Specifically, in Section IV-A, we conceptually demonstrate how CNNergy processes the 3-D data volume by dividing

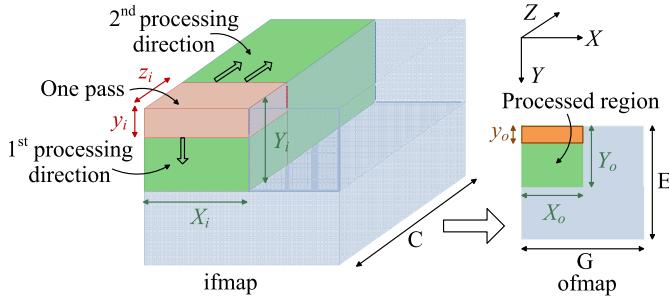


Fig. 5. Simplified schematic illustrating how CNNergy processes an ifmap (for one 3-D filter).

it into multiple subvolumes. We also define the parameters to schedule the CNN computation in this section. Next, in Section IV-B, we describe the dataflow to distribute the convolution operation in the PE array and identify the degrees of freedom to map the computation in the hardware. In Section IV-C, we present our automated mapping scheme to compute the computation scheduling parameters for any given CNN layer. Finally, using the scheduling parameters, we present the steps to compute energy for each component of (3) in Section IV-D.

A. Conceptual Illustration of CNNergy

Fig. 5 illustrates how the 3-D ifmap is processed by convolving one 3-D filter with ifmap to obtain one 2-D channel of ofmap; this is repeated over all filters to obtain all channels of ofmap. Due to the large volume of data in a CNN layer and the limited availability of on-chip storage (register files and SRAM), the data are divided into smaller subvolumes, each of which is processed by the PE array in one pass to generate psums, where the capacity of the PE array and local storage determine the amount of data that can be processed in a pass.

All psums are accumulated to produce the final ofmap entry; if only a subset of psums are accumulated, then the generated psums are said to be *irreducible*. The pink region of size $X_i \times y_i \times z_i$ shows the ifmap volume that is covered in one pass, while the green region shows the volume that is covered in multiple passes before a writeback to DRAM.

As shown in the figure (for reasons provided in Section IV-C), consecutive passes process the ifmap first in the X-direction, then in the Y-direction, and finally, in the Z-direction. After a pass, irreducible psums are written back to GLB, to be later consolidated with the remainder of the computation to build ofmap entries. After processing the full Z-direction (i.e., all the channels of a filter and ifmap), the green ofmap region of size $X_o \times Y_o$ is formed and then written back to DRAM. The same process is then repeated until the full volume of ifmap/ofmap is covered.

Fig. 5 is a simplified illustration that shows the processing of one 3-D ifmap using one 3-D filter. Depending on the amount of available register file storage in the PE array, a convolution operation using $f_i \geq 1$ filters can be performed in a pass. Furthermore, subvolumes from multiple images (i.e., N ifmaps) can be processed together, depending on the SRAM storage capacity.

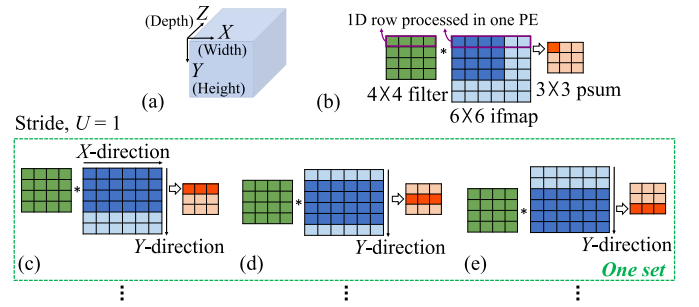


Fig. 6. (a) X-, Y-, Z-directions. (b)–(e) Example showing the convolution operation in the PEs (adapted from [27]).

Due to the high cost of data fetches, it is important to optimize the pattern of fetch operations from the DRAM, GLB, and RF by reusing the fetched data. The level of reuse is determined by the parameters f_i , z_i , y_i , y_o , X_i , X_o , Y_i , Y_o , and N . Hence, the efficiency of the computation is based on the choice of these parameters. The mapping approach that determines these parameters, in a way that attempts to minimize data movement, is described in Section IV-C.

B. Dataflow Illustration in the PE Array

In this section, we describe how the convolution operations are distributed in the 2-D PE array of size $J \times K$. We use the row-stationary scheme to manage the dataflow for convolution operations in the PE array as it is shown to offer higher energy efficiency than other alternatives [27], [28].

1) *Processing the ifmap in Sets—Concept*: We explain the row-stationary dataflow with a simplified example shown in Fig. 6, where a single channel of the filter and ifmap are processed (i.e., $z_i = 1$). Fig. 6(b) shows a basic computation, where a 4×4 filter (green region) is multiplied with the part of the ifmap that it is overlaid on, shown by the dark blue region. Based on the row-stationary scheme for the distributed computation, these four rows of the ifmap are processed in four successive PEs within a column of the PE array. Each PE performs an elementwise multiplication of the ifmap row and the filter row to create a psum. The four psums generated are transmitted to the uppermost PEs and accumulated to generate their psum (dark orange).

Extending this operation to a full convolution implies that the ifmap slides under the filter in the negative X-direction with a stride of U , while keeping the filter stationary: for $U = 1$, two strides are required to cover the ifmap in the X-direction. In our example, for each stride, each of the four PEs performs the elementwise multiplication between one filter row and one ifmap row, producing one 1-D row of psum, which is then accumulated to produce the first row of psum, as illustrated in Fig. 6(c).

Thus, the four dark blue rows in Fig. 6(c) are processed by four PEs (one per row) in a column of the PE array. The reuse of the filter avoids memory overheads due to repeated fetches from other levels of memory. To compute psums associated with other rows of the ofmap, a subarray of 12 PEs (4 rows \times 3 columns) processes the ifmap under a Y-direction ifmap stride. The ifmap regions thus processed are shown by the dark regions of Fig. 6(d) and (e).

We define the amount of processing performed in R rows, across all K columns of the PE array, as a *set*. For a 4×3 PE array, a set corresponds to the processing in Fig. 6(c)–(e).

In the general context of the $J \times K$ PE array, a set is formed from $R \times K$ PEs. Therefore, the number of sets which can fit in the full PE array (i.e., the number of sets in a pass) is given by

$$S_{\text{Pass}} = \left\lfloor \frac{J \times K}{R \times K} \right\rfloor = \left\lfloor \frac{J}{R} \right\rfloor \quad (5)$$

i.e., S_{Pass} is the ratio of the PE array height to the filter height.

2) *Processing the ifmap in Sets—Realistic Scenario*: We now generalize the previously simplified assumptions in the example to consider typical parameter ranges. We also move from the assumption of $z_i = 1$ to a more typical $z_i > 1$.

First, the filter height can often be less than the size of the PE array. When $R < J$, the remaining PE array rows can process more filter channels simultaneously, in multiple sets.

Second, typical RF sizes in each PE are large enough to operate on more than one 1-D row. Under this scenario, *within each set*, a group of 2-D filter planes is processed. There are several degrees of freedom in mapping computations to the PE array. When several 1-D rows are processed in a PE, the alternatives for choosing this group of 1-D rows include the following:

- 1) choosing filter/ifmap rows from different channels of the same 3-D filter/ifmap;
- 2) choosing filter rows from different 3-D filters;
- 3) combining 1) and 2), where some rows come from the channels of the same 3-D filter and some rows come from the channels under different 3-D filters.

Across sets in the PE array, similar mapping choices are available. Different groups of filter planes (i.e., channels) are processed in different sets. These groups of planes can be chosen either from the same 3-D filter, or from different 3-D filters, or from a combination of both.

Thus, there is a wide space of mapping choices for performing the CNN computation in the PE array.

3) *Data Reuse*: Due to the high cost of data accesses from the next memory level, it is critical to reuse data as often as possible to achieve energy efficiency. Specifically, after fetching data from a higher access-cost memory level, data reuse refers to the use of that data element in multiple MAC operations. For example, after fetching a data element from GLB to RF, if that data are used across r MAC operations, then the data are reused r times with respect to the GLB level.

We now examine the data reuse pattern within the PE array. Within each PE column, an ifmap plane is being processed along the X -direction, and multiple PE columns process the ifmap plane along the Y -direction. Two instances of data reuse in the PE array are as follows.

- 1) In each set, the *same ifmap row* is processed along the PEs in a diagonal of the set. This can be seen in the example set in Fig. 6(c)–(e), where the third row of the ifmap plane is common in the PEs in $r_3 c_1$ in (c), $r_2 c_2$ in (d), and $r_1 c_3$ in (e), where $r_i c_j$ refers to the PE in row i and column j .

TABLE II
LIST OF PARAMETERS FOR COMPUTATION SCHEDULING AND ACCELERATOR HARDWARE CONSTRAINTS

Notation	Description
Computation Scheduling Parameters	
f_i	#of filters processed in a pass
z_i	#of ifmap/filter channels processed in a pass
$y_i (y_o)$	Height of ifmap (ofmap) processed in a pass
$X_i (X_o)$	Width of ifmap (ofmap) processed in a pass
$Y_i (Y_o)$	Height of ifmap (ofmap) processed before a write back to DRAM
N	#of ifmap from different images processed together
Accelerator Hardware Parameters	
f_s	Size of RF storage for filter in one PE
I_s	Size of RF storage for ifmap in one PE
P_s	Size of RF storage for psum in one PE
J	Height of the PE array (#of rows)
K	Width of the PE array (#of columns)
$ GLB $	Size of GLB storage
b_w	bit width of each data element

- 2) The *same filter row* is processed in the PEs in a row: in Fig. 6(c)–(e), the first row of the filter plane is common to all PEs in all three columns of row 1.

Thus, data reuse can be enabled by broadcasting the same ifmap data [for instance 1)] and the same filter data [for instance 2)] to multiple PEs for MAC operations after they are fetched from a higher memory level (e.g., DRAM or GLB).

C. Obtaining Computation Scheduling Parameters

As shown in Section IV-B, depending on the specific CNN and its layer structure, there is a wide space of choices for computations to be mapped to the PE array. The mapping of filter and ifmap parameters to the PE array varies with the CNN and each layer of a CNN. This mapping is a critical issue in ensuring low energy, and therefore, in this article, we develop an automated mapping scheme for any CNN topology. The scheme computes the parameters for scheduling computations. The parameters are described in Section IV-A and summarized in Table II. Table II also includes the parameters for the accelerator hardware constraints.

For general CNNs, for each layer, we develop a mapping strategy that follows predefined rules to determine the computation scheduling. The goal of scheduling is to attempt to minimize the movement of three types of data (i.e., ifmap, psum, and filter) since data movement incurs large energy overheads. In each pass, the mapping strategy uses the following priority rules.

- 1) We process the maximum possible channels of an ifmap to reduce the number of psum terms that must move back and forth with the next level of memory.
- 2) We prioritize filter reuse, psum reduction over ifmap reuse.

The rationale for Rules 1) and 2) is that since a very large number of psums are generated in each layer, psum reduction is the most important factor for energy, particularly because transferring psums to the next pass involves expensive transactions with the next level of memory. This, in turn, implies that filter weights must remain stationary for maximal filter reuse. Criterion 2) lowers the number of irreducible

psums: if the filter is changed and ifmap is kept fixed, the generated psums are not reducible.

In processing the ifmap, proceeding along the X - and Y -directions enables the possibility of filter reuse as the filter is kept stationary in the RF while the ifmap is moved. In contrast, if passes were to proceed along the Z -direction, filter reuse would not be possible since new filter channels must be loaded from the DRAM for the convolution with ifmap. Therefore, the Z -direction is the last to be processed. In terms of filter reuse, the X - and Y -directions are equivalent, and we arbitrarily prioritize the X -direction over the Y -direction.

We use the notion of a set and a pass (Section IV-B) in the flow graph to devise the choice of scheduling parameters.

1) *Computing y_i and y_o* : The value of $y_o = \min(K, E)$ and is limited by the number of columns, K , in the PE array. The corresponding value of y_i is found using the relation

$$y_o = (y_i - R)/U + 1. \quad (6)$$

2) *Computing z_i and f_i* : The number of channels of each ifmap in a pass is computed as follows:

$$z_i = C_{\text{Set}} \times S_{\text{Pass}} \quad (7)$$

where C_{Set} is the number of channels per set, and S_{Pass} is the number of sets per pass [given by (5)]. Recall that the first priority rule of CNNergy is to process the largest possible number of ifmap channels at a time. Therefore, to compute C_{Set} , we find the number of filter rows that can fit into an ifmap RF, i.e., $C_{\text{Set}} = \lfloor I_s/S \rfloor$.

To enable per-channel convolution, the filter RF of a PE must be loaded with the same number of channels as I_s from a single filter. The remainder of the dedicated filter RF storage can be used to load channels from different filters so that one ifmap can be convolved with multiple filters resulting in ifmap reuse. Thus, after maximizing the number of channels of an ifmap/filter to be processed in a pass, the remaining f_s storage can be used to enable ifmap reuse. Therefore, the number of filters processed in a pass is

$$f_i = \lfloor f_s/I_s \rfloor. \quad (8)$$

3) *Computing X_i , X_o , Y_i , Y_o , and N* : During a pass, the ifmap corresponds to the pink region in Fig. 5, and over multiple passes, the entire green volume of the ifmap in the figure is processed before a writeback to DRAM.

We first compute $|ifmap|$ and $|psum|$, the storage requirements of ifmap and psum, respectively, during the computation. The pink region has dimension $X_i \times y_i \times z_i$ and over several passes it creates, for each of the f_i filters, a set of psums for the $X_o \times Y_o$ region of the ofmap that are not fully reduced (i.e., they await the results of more passes). Therefore,

$$|ifmap| = b_w(X_i \times y_i \times z_i) \quad (9)$$

$$|psum| = b_w(X_o \times Y_o \times f_i) \quad (10)$$

where b_w corresponds to the bit width for ifmap and psum.

Next, we determine how many ifmap passes can be processed for a limited GLB size, $|GLB|$. This is the number, N , of pink regions that can fit within the GLB, i.e.,

$$N = \left\lfloor \frac{|GLB|}{|ifmap| + |psum|} \right\rfloor. \quad (11)$$

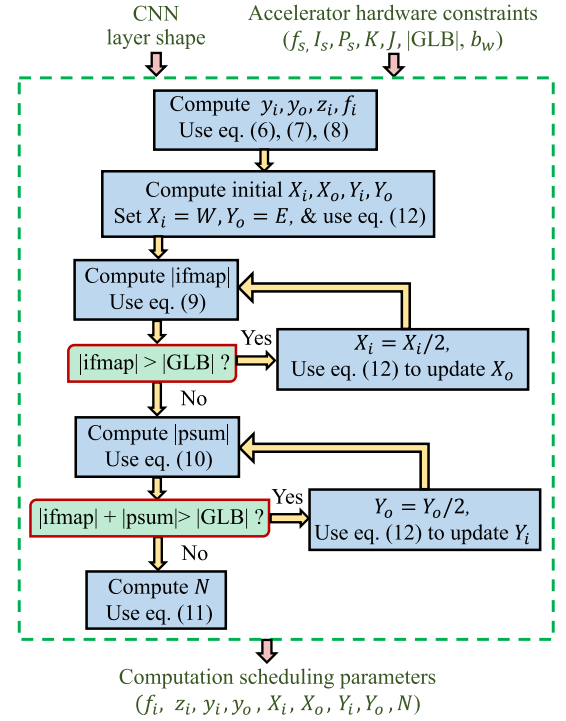


Fig. 7. Flow graph to obtain the computation scheduling parameters.

To compute X_i , we first set it to the full ifmap width, W , and we set Y_o to the full ofmap height, E , to obtain N . If $N = 0$, i.e., $|ifmap| + |psum| > |GLB|$, then X_i and Y_o are reduced until the data fit into the GLB and $N \geq 1$.

From the values of X_i and Y_o computed above, we can determine X_o and Y_i using the relations

$$X_o = \frac{X_i - S}{U} + 1; \quad Y_o = \frac{Y_i - R}{U} + 1. \quad (12)$$

Fig. 7 shows the flow graph that summarizes how the parameters for scheduling the CNN computation are computed. The module takes the CNN layer shape (Table I) and the accelerator hardware parameters (Table II) as inputs. Based on our automated mapping strategy, the module outputs the computation scheduling parameters (Table II).

4) *Exception Rules*: The mapping method handles exceptions:

- 1) If $Y_o < y_o$, some PE columns will remain unused. This is avoided by setting $Y_o = y_o$. If the new $|ifmap| + |psum| > |GLB|$, f_i is reduced so that the data fit into the GLB.
- 2) If $C < z_i$, all channels are processed in a pass while increasing f_i , as there is more room in the PE array to process more filters. The cases $F < f_i$ and $P_s < f_i$ proceed by reducing f_i .
- 3) All Conv layers whose filter has the dimension $R = S = 1$ (e.g., inside the inception modules of GoogleNet or the fire modules of SqueezeNet) are handled under a fixed exception rule that uses a reduced z_i and suitably increased f_i .

The exceptions are triggered only for a few CNN layers (i.e., layers having relatively few channels or filters).

Algorithm 1 Algorithm for Energy Computation

INPUT: Computation scheduling parameters: $f_i, z_i, y_i, y_o, X_i, X_o, Y_i, Y_o, N$ (defined in Table II);

CNN layer shape parameters: R, S, H, W, E, G, C, F (defined in Table I);

Technology parameters for energy per operation (specified in Table III)

OUTPUT: Energy to process a CNN layer, E_{Layer}

STEPS:

- 1: Determine the subvolume from each ifmap ($X_i \times y_i \times z_i$) and from each filter ($R \times S \times z_i$) processed in one pass.
- 2: Determine the number of psums ($X_o \times y_o$) generated during a pass from each 3D filter and each image.
- 3: Compute I_{Pass} , # of ifmap elements accessed in one pass from DRAM and GLB, using (13)
- 4: Compute P_{Pass} , # of psum elements to read (write) from (to) GLB during one pass, using (14)
- 5: Compute F_{Pass} , # of filter elements to load from DRAM for one pass, using (15)
- 6: Compute # of passes before a writeback of ofmap to DRAM ($\frac{Y_o}{y_o} \times \frac{C}{z_i}$ passes along Y and Z -directions)
- 7: Compute $E_{D_{X_i Y_i z_i}}$, data access energy to process a subvolume of ifmap over which filter data is reused, using (16)
- 8: Repeat Step 7 to compute $E_{D_{X_o Y_o}}$, data access energy to produce and perform DRAM write of $X_o \times Y_o$ region of each ofmap channel over f_i filters and N images, using (17)
- 9: Repeat Step 8 to compute E_{Data} , total data access energy, using (18)
- 10: Compute E_{Comp} using (19)
- 11: Compute E_{Ctrl} using (20)
- 12: Compute E_{Layer} , using (3)

TABLE III
TECHNOLOGY PARAMETERS USED FOR CNENERGY

	16-bit MAC, \tilde{e}_{MAC} 45nm [29]	Memory access, 65nm [28]			
		RF access, \tilde{e}_{RF}	Inter-PE access, \tilde{e}_{IPE}	GLB access, \tilde{e}_{GLB}	DRAM access, \tilde{e}_{DRAM}
Energy	0.95 pJ	1.69 pJ	3.39 pJ	10.17 pJ	338.82 pJ

D. Energy (E_{Layer}) Computation

In Section IV-C, we have determined the subvolume of ifmap and filter data to be processed in a pass. From the scheduling parameters, we can also compute the number of passes before a writeback of ofmap to DRAM. Therefore, we have determined the schedule of computations to generate all channels of ofmap. We now estimate each component of E_{Layer} in (3). The steps for this energy computation are summarized in Algorithm 1, which takes as input the computation scheduling parameters, CNN layer shape parameters, and technology-dependent parameters that specify the energy per operation (Table III), and outputs E_{Layer} .

1) *Computing E_{Data} , E_{Comp} :* We begin by computing the subvolume of data loaded in each pass (Lines 1–5). In Fig 5, I_{Pass} is illustrated as the pink ifmap region, which is processed in one pass for an image, and P_{Pass} is the number of psum entries associated with the orange ofmap region for a single filter and a single image. The filter data are reused across (Y_o/y_o) passes, and we denote the number of filter elements loaded for these passes by F_{Pass} . Thus, for f_i filters and N images

$$I_{\text{Pass}} = N \times (X_i \times y_i \times z_i) \quad (13)$$

$$P_{\text{Pass}} = N \times (X_o \times y_o) \times f_i \quad (14)$$

$$F_{\text{Pass}} = f_i \times (R \times S \times z_i). \quad (15)$$

To compute energy, we first determine $E_{D_{X_i Y_i z_i}}$, the data access energy required to process $X_i \times Y_i \times z_i$ volume of each

ifmap over f_i filters and N images. In each pass, a volume I_{Pass} of the ifmap is brought from the DRAM to the GLB for data access; P_{Pass} psums move between GLB and RF; and RF-level data accesses (RF_{MAC}) occur for the four operands associated with each MAC operation in a pass. Therefore, the corresponding energy can be computed as follows:

$$E_{D_{X_i Y_i z_i}} = \left[e_{\text{DRAM}}(I_{\text{Pass}}) + e_{\text{GLB}}(I_{\text{Pass}}) + e_{\text{GLB}}(P_{\text{Pass}}) + e_{\text{RF}}(\text{RF}_{\text{MAC}}) \right] \times \frac{Y_o}{y_o} + e_{\text{DRAM}}(F_{\text{Pass}}). \quad (16)$$

Here, $e_{\mathcal{O}}()$ denotes the energy associated with operation \mathcal{O} , and each energy component can be computed by multiplying the energy per operation by the number of operations. Since filter data are reused across (Y_o/y_o) passes, all components in (16), except the energy associated with filter access, are multiplied by this factor. Each psum is written once and read once, and $e_{\text{GLB}}(P_{\text{Pass}})$ accounts for both operations.

Next, all C channels of ifmap (i.e., the entire green ifmap region in Fig. 5) are processed to form the green $X_o \times Y_o$ region of each ofmap channel, and these data are written back to DRAM. To this end, we compute $E_{D_{X_o Y_o}}$, the data access energy to produce $X_o \times Y_o$ fraction of each ofmap channel over f_i filters and N images, by repeating the operations in (16) to cover all the channels

$$E_{D_{X_o Y_o}} = \left(E_{D_{X_i Y_i z_i}} \times \frac{C}{z_i} \right) + e_{\text{DRAM}}(\text{ofmap}). \quad (17)$$

Finally, the computation in (17) is repeated to produce the entire $G \times E$ volume of the ofmap over all F filters. Therefore, the total energy for data access is

$$E_{\text{Data}} = E_{D_{X_o Y_o}} \times \frac{G}{X_o} \times \frac{E}{Y_o} \times \frac{F}{f_i}. \quad (18)$$

Here, the multipliers (G/X_o), (E/Y_o), and (F/f_i) represent the number of iterations of this procedure to cover the entire ofmap. These steps are summarized in Lines 6–9 of Algorithm 1. Finally, the computation energy of the Conv layer is computed by

$$E_{\text{Comp}} = N \times (R \cdot S \cdot C) \times (E \cdot G \cdot F) \times \tilde{e}_{\text{MAC}} \quad (19)$$

where \tilde{e}_{MAC} is the energy per MAC operation, and it is multiplied by the number of MACs required for a CNN layer.

2) *Sparsity:* The analytical model exploits sparsity in the data (i.e., zeros in ifmap/ofmap) at internal layers of a CNN. Except the input ifmap to the first Conv layer of a CNN, all data communication with the DRAM (i.e., ifmap read or ofmap write) is performed in run-length compressed (RLC) format [23]. In addition, for a zero-valued ifmap, the MAC computation as well as the associated filter and psum read (write) from (to) RF level is skipped to reduce energy.

3) *Computing E_{Ctrl} :* The control overhead includes the clock power, overheads for control circuitry for the PE array, network-on-chip to manage data delivery, and I/O pads. Among these, the clock power is a major contributor (documented as ~33%–45% in [23]), and other components are relatively modest. The total control energy, E_{Ctrl} ,

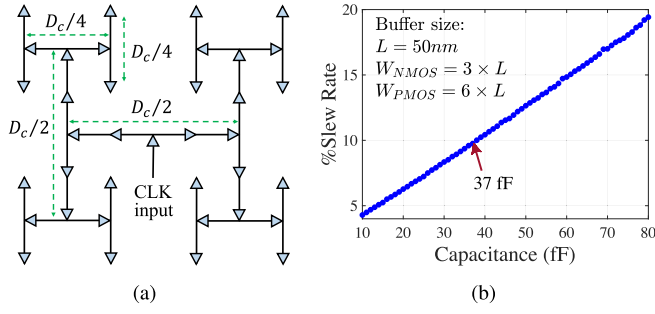


Fig. 8. (a) H-tree style clock distribution network. (b) Percent slew of the clock versus load capacitance driven by each stage of a clock buffer.

is modeled as follows:

$$E_{\text{Cntrl}} = P_{\text{clk}} \times \text{latency} \times T_{\text{clk}} + E_{\text{other-Cntrl}} \quad (20)$$

where P_{clk} is the clock power, latency is the number of cycles required to process a single layer, and T_{clk} is the clock period; $E_{\text{other-Cntrl}}$ is the control energy from components other than the clock network. We adopt similar strategy as in CACTI [14] and ORION [15] to model the power of the clock network. For a supply voltage of V_{DD} , the clock power is computed as follows:

$$P_{\text{clk}} = C_{\text{clk}} \times (V_{\text{DD}})^2 / T_{\text{clk}} + L_{\text{clk}} \quad (21)$$

$$C_{\text{clk}} = C_{\text{total-wire}} + C_{\text{total-buff}} + C_{\text{total-PEreg}} + C_{\text{SRAM}} \quad (22)$$

where L_{clk} is leakage in the clock network. The switching capacitance, C_{clk} , includes the capacitances of the global clock buffers, wires, clocked registers in the PEs, and clocked SRAM (GLB) components. We now provide details of how each component of C_{clk} is determined. We distribute the clock as a four-level H-tree shown in Fig. 8(a), where, after every two levels, the wire length reduces by a factor of 2. The total wire capacitance of the H-tree, $C_{\text{total-wire}}$, is given by

$$C_{\text{total-wire}} = \left[\frac{D_C}{2} + \left(\frac{D_C}{2} \times 2 \right) + \left(\frac{D_C}{4} \times 4 \right) + \left(\frac{D_C}{4} \times 8 \right) \right] \times C_{w/l} \quad (23)$$

where D_C is the chip dimension and $C_{w/l}$ is the per unit-length capacitance of the wire. The capacitance due to clock buffer, $C_{\text{total-buff}}$, is computed as follows:

$$C_{\text{total-buff}} = N_{\text{buff}} \times C_{\text{buff}}. \quad (24)$$

Here, N_{buff} is the number of total buffers in the H-tree and C_{buff} is the input gate capacitance of a single clock buffer. In our implementation, we chose the size and the number of the clock buffers to maintain a slew rate within 10% of T_{clk} . The $C_{\text{total-PEreg}}$ component of (22) represents the capacitance due to the clocked registers in the PEs of the accelerator and is given by

$$C_{\text{total-PEreg}} = (J \times K) \times N_{\text{FF}} \times C_{\text{FF}}. \quad (25)$$

Here, $(J \times K)$ is the PE array size, and N_{FF} is the number of 1-bit flip-flop per PE while C_{FF} denotes the clocked capacitance from a single flip-flop. The clocked capacitance from the SRAM memory, C_{SRAM} , consists of the following components:

$$C_{\text{SRAM}} = C_{\text{decod}} + C_{\text{ARW-reg}} + C_{\text{BL-pre}} + C_{\text{SA-pre}}. \quad (26)$$

Here, C_{decod} denotes the clocked capacitance from the decoder circuitry which comes from the synchronization of the word line with the clock. $C_{\text{ARW-reg}}$ is the capacitance from the clocked registers (i.e., address, read, and write registers) and computed by counting the number of flip-flops in these registers. The clocked capacitance to precharge the bit lines, $C_{\text{BL-pre}}$, is estimated from the number of total columns in the SRAM array. The precharge of each sense amplifier also needs to be synchronized with the clock, and the associated capacitance, $C_{\text{SA-pre}}$, is estimated from the number of total sense amplifiers in the SRAM array. Finally, we model $E_{\text{other-Cntrl}}$ component of (20) as 15% of E_{Layer} excluding E_{DRAM} , similar to data from the literature.

V. VALIDATION OF CNNERGY

We validate CNNergy against limited published data for AlexNet and GoogleNet-v1:

- 1) EyMap, the Eyeriss energy model, utilizing the mapping parameters provided in [23]. These data *only provide parameters for the five Conv layers of AlexNet*.
- 2) EyTool, Eyeriss's energy estimation tool [30], excludes E_{Cntrl} and *supports AlexNet and GoogleNet-v1 only*.
- 3) EyChip, measured data from 65-nm silicon [23] (*AlexNet Conv layers only, excludes E_{DRAM}*).

Note that our CNNergy exceeds the capability of these:

- 1) CNNergy is suitable for customized energy access (i.e., any intermediate CNN energy component is obtainable).
- 2) CNNergy can find energy for various accelerator parameters.
- 3) CNNergy can analyze a vast range of CNN topologies and general CNN accelerators, not just Eyeriss.

To enable a direct comparison with Eyeriss, 16-bit fixed point arithmetic precision is used to represent feature maps and filter weights. The technology parameters are listed in Table III. The available process data are from 45- and 65-nm nodes, and we use the factor $s = (65/45) \times (V_{\text{DD},65\text{ nm}} / V_{\text{DD},45\text{ nm}})^2$ to scale 45-nm data for direct comparison with measured 65-nm silicon.

For the control energy, we model capacitances using the parameters from the NCSU 45-nm process design kit (PDK) [31]; the capacitive components in (22)–(26) are extracted to estimate C_{clk} . Fig. 8(b) shows the percent slew of the clock as we increase the load capacitance to a single clock buffer (MOSFET sizing of the buffer: length, $L = 50\text{ nm}$; width, $W_{\text{NMOS}} = 3L$ and $W_{\text{PMOS}} = 6L$). From this plot, the maximum load capacitance to each clock buffer (37 fF) is calculated to maintain a maximum of 10% slew rate, and the buffers in the H-tree are placed accordingly. The results are scaled to 65-nm node by the scaling factor s . The resultant clock power is computed by (21), and the latency for each layer in (20) is inferred as $(\# \text{ of MAC per layer} / \text{Throughput})$, where the numerator is a property of the CNN topology and the denominator is obtained from [23].

Fig. 9(a) shows the comparison of the energy obtained from CNNergy, EyTool, and EyMap to process an input image for AlexNet. As stated earlier, EyTool excludes E_{Cntrl} ; accordingly, our comparison also omits E_{Cntrl} . The numbers match closely.

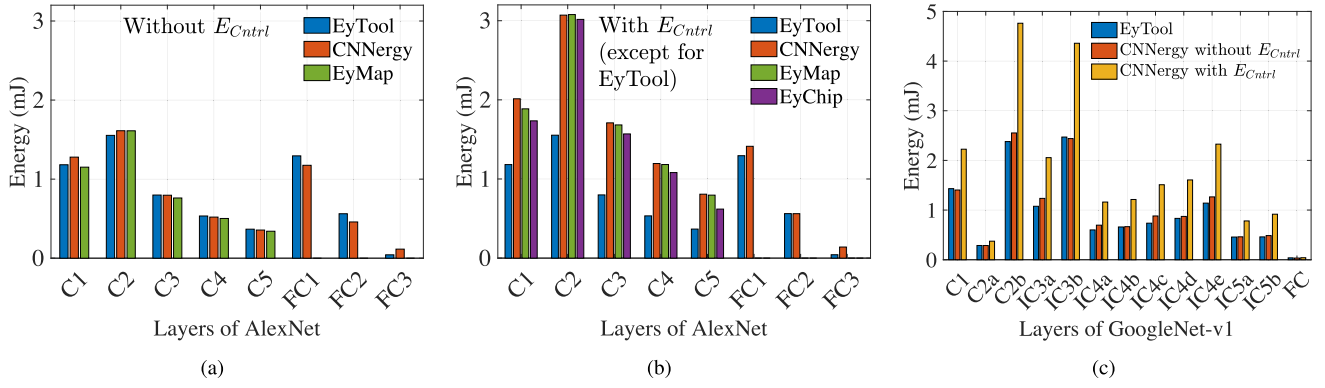


Fig. 9. Energy validation of CNNergy: (a) AlexNet without E_{Cntrl} , (b) AlexNet with E_{Cntrl} model, and (c) GoogleNet-v1.

Fig. 9(b) shows the energy results for AlexNet including the E_{Cntrl} component in (3) for both CNNergy and EyMap and compares the results with EyChip which represents practical energy consumption from a fabricated chip. The EyTool data that neglect E_{Cntrl} are significantly off from the more accurate data for CNNergy, EyMap, and EyChip, particularly in the Conv layers. Due to unavailability of reported data, the bars in Fig. 9(b) only show the Conv layer energy for EyMap and EyChip. Note that EyChip does not include the E_{DRAM} component of (4).

Fig. 9(c) compares the energy from CNNergy with the EyTool energy for GoogleNet-v1. Note that the only available hardware data for GoogleNet-v1 is from EyTool, which does not report control energy: this number matches the non- E_{Cntrl} component of CNNergy closely. As expected, the energy is higher when E_{Cntrl} is included.

VI. TRANSMISSION ENERGY AND DELAY COMPUTATION

A. Transmission Energy (E_{Trans}) Estimation

The transmission energy, E_{Trans} , is a function of the available data bandwidth, which may vary depending on the environment that the mobile client device is in. Similar to the prior works on offloading computation to the cloud [12], [20], [32], we use the following model to estimate the energy required to transmit data bits from the mobile client to the cloud:

$$E_{Trans} = P_{Tx} \times \frac{D_{RLC}}{B_e} \quad (27)$$

where P_{Tx} is the transmission power of the client, B_e is the effective transmission bit rate, and D_{RLC} is the number of encoded data bits to be transmitted. The time required to transmit the data bits is determined by the bit rate. Similar to [33], the transmission power is assumed to be constant during the course of transmission after the wireless connection has been established as well as a simple fading environment is assumed. During data transmission, typically, there is an overhead due to error correction scheme. An error correction code (ECC) effectively reduces the data bandwidth. If $k\%$ of the actual data is designated for the ECC bits, then the effective transmission bit rate for actual data [i.e., D_{RLC} in (27)] is given by

$$B_e = \frac{B}{1 + (k/100)} \quad (28)$$

where B is the available transmission bit rate. For the highly sparse data at internal layers of a CNN, run-length

compression (RLC) encoding is used to reduce the transmission overhead. The number of transmitted RLC encoded data bits, D_{RLC} , is

$$D_{RLC} = D_{raw} \times (1 - Sparsity) \times (1 + \delta). \quad (29)$$

Here, D_{raw} is the number of output data bits at each layer including zero elements, $Sparsity$ is the fraction of zero elements in the respective data volume, and δ is the average RLC encoding overhead for each bit associated with the nonzero elements in the raw data [i.e., to encode each bit of a nonzero data element, on average, $(1 + \delta)$ bits are required]. Using 4-bit RLC encoding (i.e., to encode information about the number of zeros between nonzero elements) for 8-bit data (for evaluations in Section VIII), and 5-bit RLC encoding for 16-bit data (during Eyeriss validation in Section V), δ is 3/5 and 1/3, respectively (note that this overhead only applies to the few nonzeros in a very sparse data).

B. Inference Delay (t_{delay}) Estimation

Although our framework aims to optimize client energy, we also evaluate the total time required to complete an inference (t_{delay}) in the client+cloud. For a computation partitioned at the L^{th} layer, the inference delay is modeled as follows:

$$t_{delay} = \sum_{i=1}^L t_{client}(i) + t_{Trans} + \sum_{i=L+1}^{|L|} t_{cloud}(i) \quad (30)$$

where $t_{client}(i)$ [$t_{cloud}(i)$] denote the i^{th} layer latency at the client [cloud], $|L|$ is the number of layers in the CNN, and $t_{Trans} = D_{RLC}/B_e$ is the time required for data transmission at the L^{th} layer. The latency for each layer is computed as in Section V, where the Throughput comes from the client and cloud platforms.

VII. RUNTIME PARTITIONING BY NEUPART

In this section, we discuss how NeuPart is used during runtime for partitioning CNN workloads between a mobile client and the cloud. Fig. 10 shows the average (μ) and standard deviation (σ) of data sparsity at various CNN layers over $\sim 10,000$ ImageNet validation images for AlexNet, SqueezeNet-v1.1, GoogleNet-v1, and VGG-16. For all four networks, the standard deviation of sparsity at all layers is an order of magnitude smaller than the average. However,

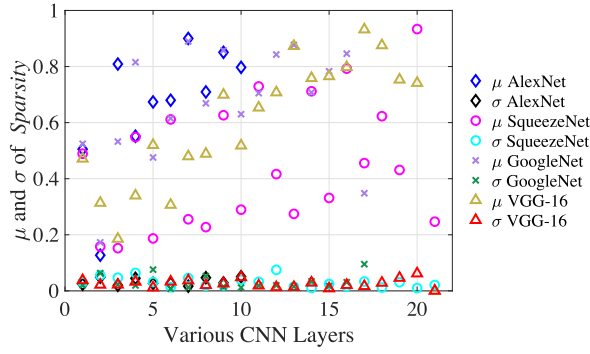


Fig. 10. Average (μ) and standard deviation (σ) of *Sparsity* over $\sim 10,000$ images for AlexNet, SqueezeNet-v1.1, GoogleNet-v1, and VGG-16.

Algorithm 2 Algorithm for Runtime Optimal Partitioning

INPUT: $E \in \mathbb{R}^{|L|}$: Cumulative CNN energy vector;
 $D_{\text{RLC}} \in \mathbb{R}^{|L|}$: RLC encoded data bits for various layers;
 B : Available transmission bit rate; P_{Tx} : Transmission power;
 k : Percent overhead for ECC bits
OUTPUT: Optimal partition layer, L_{opt}
METHOD:
1: Obtain JPEG compressed image sparsity, *Sparsity-In*
2: Update RLC data size for input layer, D_{RLC}^1 using *Sparsity-In* and (29)
3: Compute $B_e = \frac{B}{1+(k/100)}$
4: Compute $E_{\text{Trans}}^L = P_{\text{Tx}} \times \frac{D_{\text{RLC}}^L}{B_e}$, $L \in \{1, 2, \dots, |L|\}$
5: Compute $E_{\text{Cost}}^L = E_L + E_{\text{Trans}}^L$, $L \in \{1, 2, \dots, |L|\}$
6: Obtain $L_{\text{opt}} = \text{argmin}(E_{\text{Cost}})$
7: **return** L_{opt}

at the input layer, when the image is transmitted in standard JPEG compressed format, the sparsity of the JPEG compressed image, *Sparsity-In*, shows significant variation (documented in Fig. 12), implying that the transmit energy can vary significantly.

Therefore, a significant observation is that for all the intermediate layers, *Sparsity* is primarily a feature of the network and not the input data, and can be precomputed offline as a standard value, independent of the input image. This implies that D_{RLC} , which depends on *Sparsity*, can be computed offline for all the intermediate layers without incurring any optimality loss on the partitioning decision. Only for the input layer, it is necessary to compute D_{RLC} during runtime. The runtime optimization algorithm is, therefore, very simple and summarized in Algorithm 2 (for notational convenience, we use superscript/subscript L to indicate L^{th} layer in this algorithm).

The cumulative CNN energy vector (E) up to each L^{th} layer of a CNN [i.e., $E_L = \sum_{i=1}^L E_{\text{Layer}}(i)$] depends on the network topology and, therefore, precomputed offline by CNNergy. Likewise, D_{RLC} for layer 2 to $|L|$ is precharacterized using the average *Sparsity* value associated with each CNN layer. During runtime, for an input image with JPEG-compressed sparsity *Sparsity-In*, D_{RLC} for layer 1 (i.e., input layer) is computed (Line 2). Finally, at runtime, with a user-specified transmission bit rate B , percent ECC overhead k , and transmission power P_{Tx} , E_{Cost} is obtained for all the layers, and the layer that minimizes E_{Cost} is selected as the optimal partition point, L_{opt} (Lines 4–7).

Note that both B and P_{Tx} are user-specified parameters in the runtime optimization algorithm. Therefore, depending on

the communication environment (i.e., signal strength, quality of the link, amount of contention from other users, and variable bandwidth), a user can provide the available bit rate. In addition, depending on a specific device, the user can provide the transmission power corresponding to that device and obtain the partitioning decision based on the provided B and P_{Tx} parameters at runtime.

Overhead of Runtime Optimization: The computation of Algorithm 2 requires only $(|L| + 1)$ multiplications, $(|L| + 2)$ divisions, $(|L| + 2)$ additions, and $|L|$ comparison operations (Lines 2–6), where $|L|$ is the number of layers in the CNN topology. For standard CNNs, $|L|$ is a very small number (e.g., for AlexNet, GoogleNet-v1, SqueezeNet-v1.1, and VGG-16, $|L|$ lies between 12 and 22). This makes NeuPart computationally very cheap to find the optimal partition layer at runtime. Moreover, as compared to the energy required to perform the core CNN computations and data transmission, the overhead of running Algorithm 2 is virtually zero.

Note that the inference result returned from the cloud computation corresponds to a trivial amount of data (i.e., only one number associated with the identified class) which is, for example, five orders of magnitude lower than the number of data bits to transmit at the P2 layer of AlexNet [already very low, see Fig. 2(b)]. Therefore, the cost of receiving the result makes no perceptible difference in the partitioning decision.

VIII. RESULTS

A. In Situ/Cloud Partition

We now evaluate the computational partitioning scheme, using the models in Sections IV and VI. Similar to the state-of-the-art [1], [34], we use 8-bit inference for our evaluation. The energy parameters from Table III are quadratically scaled for multiplication and linearly scaled for addition and memory access to obtain 8-bit energy parameters. We compare the results of partitioning with the following:

- 1) FCC: fully cloud-based computation;
- 2) FISC: fully *in situ* computation on the client.

The energy cost (E_{Cost}) in (1) for each layer of a CNN is analyzed under various communication environments for the mobile cloud-connected client. Prior works in the literature [35]–[37] report the measured average power of various smartphones during the uplink activity of wireless network (documented in Table IV). In this work, for the transmission power (P_{Tx}) in (27), we use representative numbers from Table IV and, thus, evaluate the computational partitioning scheme considering specific scenarios that correspond to specific mobile platforms. The transmit power for an on-chip transmitter is independent of the transmission data rate [33], and the numbers in Table IV do not vary with the data rate. We present analysis using the effective bit rate (B_e) as a variable parameter to evaluate the benefit from the computation partitioning scheme as the available bandwidth changes. For all plots: 1) “In” is the input layer (i.e., the input image data); 2) layers starting with “C,” “P,” and “FC” denote Conv, Pool, and FC layers, respectively; and 3) layers starting with “Fs” and “Fe” denote *squeeze* and *expand* layers, respectively, inside a fire module of SqueezeNet-v1.1.

TABLE IV
MEASURED AVERAGE POWER OF SMARTPHONES DURING
WIRELESS NETWORK UPLINK ACTIVITY

Wireless network	WLAN	3G	4G LTE
Google Nexus One [35]	—	0.45 W	—
LG Nexus 4 [36]	0.78 W	0.71 W	—
Samsung Galaxy S3 [36]	0.85 W	1.13 W	1.13 W
BlackBerry Z10 [36]	1.14 W	1.03 W	1.22 W
Samsung Galaxy Note 3 [36]	1.28 W	0.75 W	2.3 W
Nokia N900 [37]	1.1 W	1.0 W	—

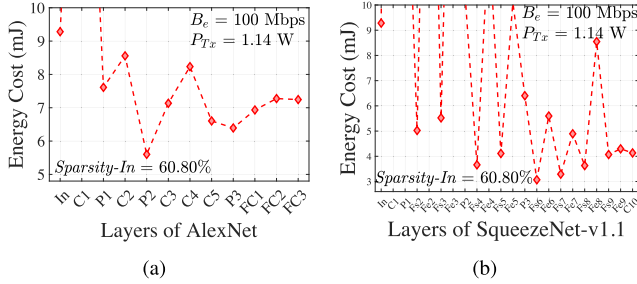


Fig. 11. Energy cost (E_{Cost}) at various layers for (a) AlexNet and (b) SqueezeNet-v1.1. (In both figures, points above 10 mJ are omitted for better visibility.)

At the In layer, before transmission, the image is JPEG-compressed with a quality level of $Q = 90$ (a lower Q provides greater compression but the worsened image induces CNN accuracy degradation). The energy overhead associated with JPEG compression [38] is incorporated in E_{Cost} for the In layer but is negligible.

For an input image, Fig. 11(a) shows the energy cost associated with each layer of AlexNet at 100 Mbps effective bit rate (B_e) and 1.14 W transmission power (P_{Tx}), which corresponds to the BlackBerry Z10 platform. The minimum E_{Cost} occurs at an intermediate layer, P2, of AlexNet, which is 39.65% energy-efficient than the In layer (FCC) and 22.7% energy-efficient than the last layer (FISC). It is now clear that offloading data at an intermediate layer is more energy-efficient for the client than FCC or FISC. Using the same smartphone platform, Fig. 11(b) shows a similar result with an intermediate optimal partitioning layer for SqueezeNet-v1.1. Here, the Fs6 layer is optimal with an energy efficiency of 66.9% and 25.8% as compared to FCC and FISC, respectively.

The cost of FCC is image-dependent and varies with the sparsity, Sparsity-In , of the compressed JPEG image, which alters the transmission cost to the cloud. Fig. 12 shows that the ~ 5500 test images in the ImageNet database show large variations in Sparsity-In . We divide this distribution into four quartiles, delimited at points Q_1 , Q_2 , and Q_3 .

For representative images whose sparsity corresponds to Q_1 , Q_2 , and Q_3 , Fig. 13 shows the energy savings on the client at the optimal partition of AlexNet, as compared to FCC (left axis) and FISC (right axis). For various effective bit rates (B_e), the plots correspond to two different P_{Tx} of 0.78 and 1.28 W, corresponding to the specifications of LG Nexus 4 and Samsung Galaxy Note 3, respectively, in Table IV.

In Fig. 13, a 0% saving with respect to FCC [FISC] indicates the region where the In [output] layer is optimal

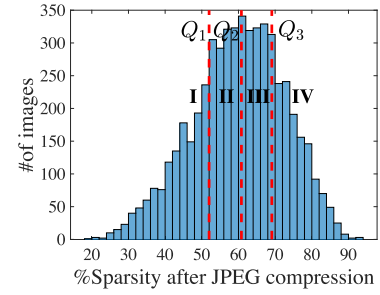


Fig. 12. Distribution of images with respect to Sparsity-In .

implying that FCC [FISC] is the most energy-efficient choice. Fig. 13(a) and (b) show that for a wide range of communication environments, the optimal layer is an intermediate layer and provides significant energy savings as compared to both FCC and FISC. However, this also depends on image sparsity: a higher value of Sparsity-In makes FCC more competitive or even optimal, especially for images in quartile IV [Fig. 13(c)]. However, for many images in the I–III quartiles, there is a large space where offloading neural computation at the intermediate optimal layer is energy-optimal.

The effect of change in P_{Tx} can also be seen from the plots in Fig. 13. With a higher value of P_{Tx} (the dotted curves), data transmission requires more energy. Therefore, the region for which an intermediate partitioning offers energy savings (i.e., the region between energy savings of 0% with respect to FCC and 0% with respect to FISC) exhibits a right shift, along with a reduction in the savings with respect to FISC. However, the region also becomes wider since with a higher P_{Tx} , FCC becomes less competitive. With the highest P_{Tx} settings from Table IV (i.e., 2.3 W), it turns out that intermediate optimal partitioning offers limited savings with respect to FISC for a lower bit rate, and from a higher bit rate (i.e., > 100 Mbps), the savings starts to become considerable. Similar trends are seen for SqueezeNet-v1.1, where the ranges of B_e for which an intermediate layer is optimal are even larger than AlexNet with higher energy savings.

The optimum partition is often, but not always, at an intermediate point for all CNNs. For example, for GoogleNet-v1, a very deep CNN, in many cases either FCC or FISC, is energy-optimal, due to the large amount of computation as well as the comparatively higher data dimension associated with its intermediate layers. However, for smaller Sparsity-In values (i.e., images which do not compress well), the optimum can indeed occur at an intermediate layer, implying energy savings by the client/cloud partitioning. For VGG-16, the optimal solution is FCC, rather than partial on-board computation or FISC. This is not surprising: VGG-16 incurs high computation cost and has large data volume in the deeper layers, resulting in high energy for client-side processing.

Under a fixed transmission power (corresponding to the platforms of LG Nexus 4 and Samsung Galaxy Note 3) and bit rate, Table V reports the average energy savings at the optimal layer as compared to FCC and FISC for all the images lying in quartiles I–IV, specified in Fig. 12. Note that the savings with respect to FISC do not depend on Sparsity-In . The shaded regions in Table V indicate the regions where energy saving

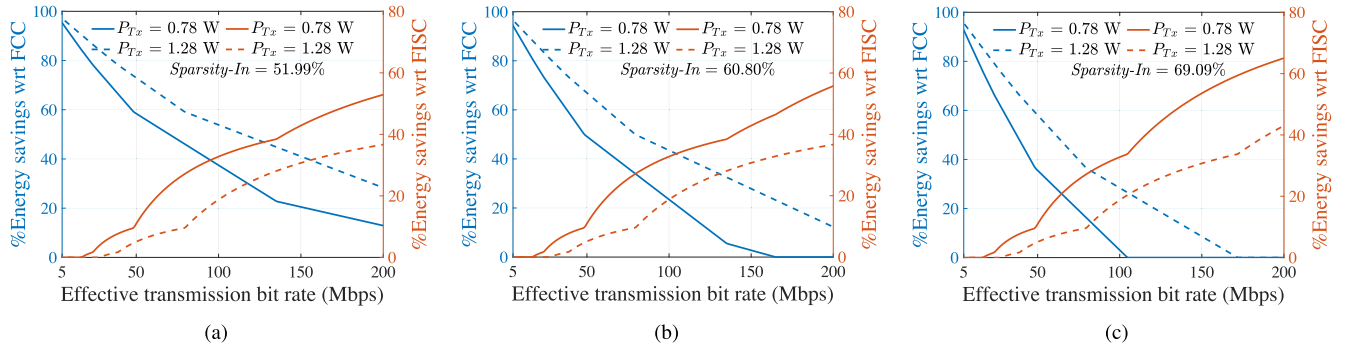


Fig. 13. Percentage energy savings of the client device under different communication environment for AlexNet at (a) $Sparsity-In = 51.99\%$ (Q_1), (b) $Sparsity-In = 60.80\%$ (Median, Q_2), and (c) $Sparsity-In = 69.09\%$ (Q_3).

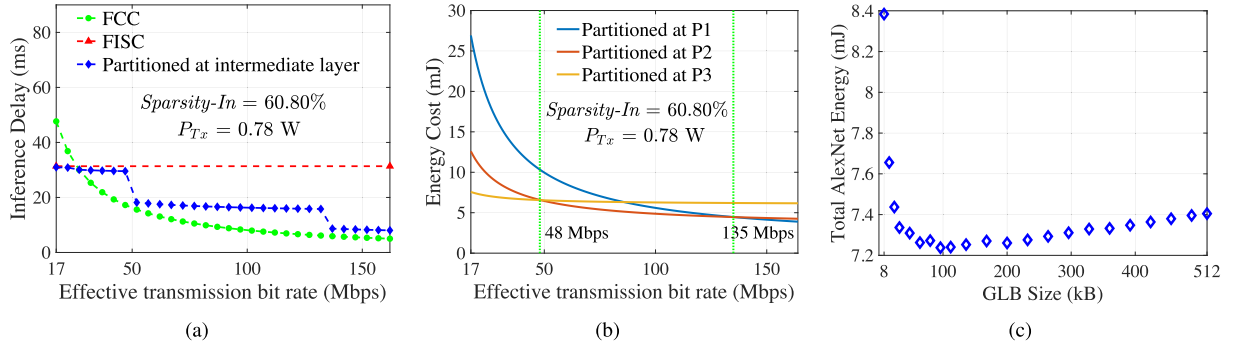


Fig. 14. Evaluations on AlexNet: (a) Inference delay (t_{delay}) with respect to FCC and FISC while partitioned at energy-optimal intermediate layers. (b) Energy cost with variation in effective bit rate (B_e) when partitioned at P1, P2, and P3 layers. (c) Total AlexNet energy versus GLB size.

TABLE V

ENERGY SAVINGS AT OPTIMAL LAYER FOR DIFFERENT CNN TOPOLOGIES ($B_e = 80$ MBPS; $P_{TX} = 0.78$ W FOR ALEXNET AND SQUEEZE NET-V1.1, 1.28 W FOR GOOGLNET-V1)

Average percent energy savings with respect to					FISC
CNN	FCC				
	Quartile				
	I	II	III	IV	
AlexNet	52.4%	40.1%	25.7%	4.1%	27.3%
SqueezeNet	73.4%	66.5%	58.4%	38.4%	28.8%
GoogleNet	21.4%	3.5%	0.0%	0.0%	10.6%

is obtained by the client/cloud partitioning. For AlexNet, the optimum occurs at an intermediate layer mostly for the images in quartiles I–III while providing up to 52.4% average energy savings. For SqueezeNet-v1.1, in all four quartiles, most images show an optimum at an intermediate layer and provide up to 73.4% average energy savings on the client.

1) *Evaluation of Inference Delay*: To evaluate the inference delay (t_{delay}), we use GoogleTPU [1], a widely deployed DNN accelerator in datacenters, as the cloud platform, with t_{cloud} in (30) use Throughput = 92 TeraOps/s. At the median $Sparsity-In$ value (Q_2), Fig. 14(a) compares the t_{delay} of energy-optimal partitioning of AlexNet with FCC and FISC for various effective bit rate. The delay of FISC does not depend on the communication environment and exhibits a constant value, whereas the delay of FCC reduces with a higher bit rate. The range of B_e for which an intermediate layer becomes energy-optimal is extracted using Q_2 [Fig. 13(b)]. The blue curve in Fig. 14(a) shows the inference delay when partitioned at those energy-optimal intermediate layers. At 49 and 136 Mbps, the curve shows a step reduction in delay since

at these points, the optimal layer shifts from P3 to P2 and P2 to P1, respectively. It is evident from the figure that in terms of inference delay, energy-optimal intermediate layers are either better than FCC (lower bit rate) or closely follow FCC (higher bit rate) and most cases are better than FISC.

2) *Impact of Variations in B* : We have analyzed the impact of changes in the available bandwidth B (e.g., due to network crowding) on the optimal partition point. For an image with $Sparsity-In$ of Q_2 and 0.78 W P_{TX} , Fig. 14(b) shows the energy cost of AlexNet when partitioned at P1, P2, and P3 layers (the candidate layers for an intermediate optimal partitioning). It shows that the energy valley is very flat with respect to bit rate when the minimum E_{Cost} shifts from P3 to P2 and P2 to P1 (the green vertical lines). Therefore, changes in bit rate negligibly change energy gains from computational partitioning. For example, in Fig. 14(b), layer P3 is optimal for $B_e = 17$ –48 Mbps, layer P2 is optimal for $B_e = 49$ –135 Mbps, and layer P1 is optimal for $B_e = 136$ –164 Mbps. However, if B_e changes from 130 to 145 Mbps, even though the optimal layer changes from P2 to P1, the energy for partitioning at P2 instead of P1 is virtually the same.

B. Design Space Exploration Using CNNergy

We show how our analytical CNN energy model (CNNergy) in Section IV can be used to perform design space exploration of the CNN hardware accelerator. For the 8-bit inference on an AlexNet workload, Fig 14(c) shows the total energy as a function of the global SRAM buffer (GLB) size. The GLB energy versus size trend was extracted using CACTI [39].

When the GLB size is low, data reuse becomes difficult since the GLB can only hold a small chunk of ifmap and psum

at a time. This leads to much higher total energy. As the GLB size is increased, data reuse improved until it saturates. Beyond a point, the energy increases due to higher GLB access cost. The minimum energy occurs at a size of 88 kB. However, a good engineering solution is 32 kB because it saves 63.6% memory cost over the optimum, with only a 2% optimality loss. Our CNNEnergy supports similar design space exploration for other accelerator parameters as well.

IX. CONCLUSION

In order to best utilize the battery-limited resources of a cloud-connected mobile client, this article presents an energy-optimal DL scheme that uses partial *in situ* execution on the mobile platform, followed by data transmission to the cloud. An accurate analytical model for CNN energy (CNNEnergy) has been developed by incorporating implementation-specific details of a DL accelerator architecture. To estimate the energy for any CNN topology on this accelerator, an automated computation scheduling scheme is developed, and it is shown to match the performance of the layerwise ad hoc scheduling approach of prior work [23]. The analytical framework is used to predict the energy-optimal partition point for mobile client at runtime, while executing CNN workloads, with an efficient algorithm. The *in situ*/cloud partitioning scheme is also evaluated under various communication scenarios. The evaluation results demonstrate that there exists a wide communication space for AlexNet and SqueezeNet, where energy-optimal partitioning can provide remarkable energy savings on the client.

REFERENCES

- [1] N. P. Jouppi et al., "In-datacenter performance analysis of a tensor processing unit," in *Proc. ISCA*, Jun. 2017, pp. 1–12.
- [2] K. Lee. (2017). *Introducing Big Basin: Our Next-generation AI Hardware*. [Online]. Available: <https://tinyurl.com/y9jh469b>.
- [3] A. Esteva et al., "Dermatologist-level classification of skin cancer with deep neural networks," *Nature*, vol. 542, no. 7639, pp. 115–118, Feb. 2017.
- [4] S. P. Mohanty, D. P. Hughes, and M. Salathé, "Using deep learning for image-based plant disease detection," *Frontiers Plant Sci.*, vol. 7, p. 1419, Sep. 2016.
- [5] S.-J. Hong, Y. Han, S.-Y. Kim, A.-Y. Lee, and G. Kim, "Application of deep-learning methods to bird detection using unmanned aerial vehicle imagery," *Sensors*, vol. 19, no. 7, p. 1651, Apr. 2019.
- [6] A. Krizhevsky, I. Sutskever, and G. E. Hinton, "Imagenet classification with deep convolutional neural networks," in *Proc. Adv. Neural Inf. Process. Syst. (NIPS)*, 2012, pp. 1097–1105.
- [7] H. Li, K. Ota, and M. Dong, "Learning IoT in edge: Deep learning for the Internet of Things with edge computing," *IEEE Netw.*, vol. 32, no. 1, pp. 96–101, Jan. 2018.
- [8] C. Hu, W. Bao, D. Wang, and F. Liu, "Dynamic adaptive DNN surgery for inference acceleration on the edge," in *Proc. IEEE INFOCOM Conf. Comput. Commun.*, Apr. 2019, pp. 1423–1431.
- [9] H. Li, C. Hu, J. Jiang, Z. Wang, Y. Wen, and W. Zhu, "JALAD: Joint accuracy- and latency-aware deep structure decoupling for edge-cloud execution," in *Proc. IEEE 24th Int. Conf. Parallel Distrib. Syst. (ICPADS)*, Dec. 2018, pp. 671–678.
- [10] H.-J. Jeong, H.-J. Lee, C. H. Shin, and S.-M. Moon, "IONN: Incremental offloading of neural network computations from mobile devices to edge servers," in *Proc. ACM Symp. Cloud Comput.*, Oct. 2018, pp. 401–411.
- [11] A. E. Eshratifar and M. Pedram, "Energy and performance efficient computation offloading for deep neural networks in a mobile cloud computing environment," in *Proc. Great Lakes Symp. VLSI*, May 2018, pp. 111–116.
- [12] Y. Kang et al., "Neurosurgeon: Collaborative intelligence between the cloud and mobile edge," in *Proc. ASPLOS*, 2017, pp. 615–629.
- [13] D. Brooks, V. Tiwari, and M. Martonosi, "Watch: A framework for architectural-level power analysis and optimizations," in *Proc. 27th Int. Symp. Comput. Archit.*, 2000, pp. 83–94.
- [14] S. J. E. Wilton and N. P. Jouppi, "CACTI: An enhanced cache access and cycle time model," *IEEE J. Solid-State Circuits*, vol. 31, no. 5, pp. 677–688, May 1996.
- [15] A. B. Kahng, B. Li, L.-S. Peh, and K. Samadi, "ORION 2.0: A fast and accurate NoC power and area model for early-stage design space exploration," in *Proc. Design, Autom. Test Eur. Conf. Exhibit.*, Apr. 2009, pp. 423–428.
- [16] F. N. Iandola, S. Han, M. W. Moskewicz, K. Ashraf, W. J. Dally, and K. Keutzer, "SqueezeNet: AlexNet-level accuracy with 50x fewer parameters and <0.5MB model size," 2016, *arXiv:1602.07360*. [Online]. Available: <http://arxiv.org/abs/1602.07360>
- [17] K. Simonyan and A. Zisserman, "Very deep convolutional networks for large-scale image recognition," 2014, *arXiv:1409.1556*. [Online]. Available: <http://arxiv.org/abs/1409.1556>
- [18] C. Szegedy et al., "Going deeper with convolutions," in *Proc. IEEE Conf. Comput. Vis. Pattern Recognit. (CVPR)*, Jun. 2015, pp. 1–9.
- [19] B. Zhang, A. Davoodi, and Y. H. Hu, "Exploring energy and accuracy tradeoff in structure simplification of trained deep neural networks," *IEEE J. Emerg. Sel. Topics Circuits Syst.*, vol. 8, no. 4, pp. 836–848, Dec. 2018.
- [20] K. Kumar and Y.-H. Lu, "Cloud computing for mobile users: Can offloading computation save energy?" *Computer*, vol. 43, no. 4, pp. 51–56, Apr. 2010.
- [21] T. Chen et al., "A high-throughput neural network accelerator," *IEEE Micro*, vol. 35, no. 3, pp. 24–32, May 2015.
- [22] Z. Du et al., "ShiDianNao: Shifting vision processing closer to the sensor," in *Proc. ISCA*, Jun. 2015, pp. 92–104.
- [23] Y.-H. Chen, T. Krishna, J. S. Emer, and V. Sze, "Eyeriss: An energy-efficient reconfigurable accelerator for deep convolutional neural networks," *IEEE J. Solid-State Circuits*, vol. 52, no. 1, pp. 127–138, Jan. 2017.
- [24] H. Sharma et al., "Bit fusion: Bit-level dynamically composable architecture for accelerating deep neural network," in *Proc. ACM/IEEE 45th Annu. Int. Symp. Comput. Archit. (ISCA)*, Jun. 2018, pp. 764–775.
- [25] A. Aïmar et al., "NullHop: A flexible convolutional neural network accelerator based on sparse representations of feature maps," *IEEE Trans. Neural Netw. Learn. Syst.*, vol. 30, no. 3, pp. 644–656, Mar. 2019.
- [26] J. Sim, J.-S. Park, M. Kim, D. Bae, Y. Choi, and L.-S. Kim, "14.6 A 1.42TOPS/W deep convolutional neural network recognition processor for intelligent IoE systems," in *IEEE Int. Solid-State Circuits Conf. (ISSCC) Dig. Tech. Papers*, Jan. 2016, pp. 264–265.
- [27] V. Sze, Y.-H. Chen, T.-J. Yang, and J. S. Emer, "Efficient processing of deep neural networks: A tutorial and survey," *Proc. IEEE*, vol. 105, no. 12, pp. 2295–2329, Dec. 2017.
- [28] Y.-H. Chen, J. Emer, and V. Sze, "Eyeriss: A spatial architecture for energy-efficient dataflow for convolutional neural networks," in *Proc. ACM/IEEE 43rd Annu. Int. Symp. Comput. Archit. (ISCA)*, Jun. 2016, pp. 367–379.
- [29] M. Horowitz, "1.1 Computing's energy problem (and what we can do about it)," in *IEEE Int. Solid-State Circuits Conf. (ISSCC) Dig. Tech. Papers*, Feb. 2014, pp. 10–14.
- [30] *Deep Neural Network Energy Estimation Tool*. Accessed: Mar. 12, 2020. [Online]. Available: <https://energyestimation.mit.edu>
- [31] *NCSU FreePDK45*. Accessed: Mar. 12, 2020. [Online]. Available: <https://www.eda.ncsu.edu/wiki/>
- [32] Y. Nimmagadda, K. Kumar, and Y.-H. Lu, "Energy-efficient image compression in mobile devices for wireless transmission," in *Proc. IEEE Int. Conf. Multimedia Expo*, Jun. 2009, pp. 1278–1281.
- [33] D. Halperin, B. Greenstein, A. Sheth, and D. Wetherall, "Demystifying 802.11n power consumption," in *Proc. Int. Conf. Power Aware Comput. Syst.*, 2010, p. 1.
- [34] P. Gysel, M. Motamedi, and S. Ghiasi, "Hardware-oriented approximation of convolutional neural networks," 2016, *arXiv:1604.03168*. [Online]. Available: <http://arxiv.org/abs/1604.03168>
- [35] F. Qian, Z. Wang, A. Gerber, Z. Mao, S. Sen, and O. Spatscheck, "Profiling resource usage for mobile applications: A cross-layer approach," in *Proc. 9th Int. Conf. Mobile Syst., Appl., Services (MobiSys)*, 2011, pp. 321–334.
- [36] M. Altamimi, A. Abdrabou, K. Naik, and A. Nayak, "Energy cost models of smartphones for task offloading to the cloud," *IEEE Trans. Emerg. Topics Comput.*, vol. 3, no. 3, pp. 384–398, Sep. 2015.
- [37] A. P. Miettinen and J. K. Nurminen, "Energy efficiency of mobile clients in cloud computing," in *Proc. HotCloud*, 2010, p. 19.
- [38] F. S. Snigdha, D. Sengupta, J. Hu, and S. S. Sapatnekar, "Optimal design of JPEG hardware under the approximate computing paradigm," in *Proc. 53rd Annu. Design Autom. Conf. (DAC)*, 2016, pp. 1–6.
- [39] *CACTI*. Accessed: Mar. 12, 2020. [Online]. Available: <http://www.hpl.hp.com/research/cacti/>